

Level 2 Photometric Calibration for the LSST Survey

The Photometric Calibration Team

ABSTRACT

This document describes the photometric calibration procedure for LSST Data Release catalogs. This procedure will use specialized hardware (an auxiliary telescope and narrow-band dome screen projector) to measure the wavelength dependence of the atmospheric and hardware response functions, together with a self-calibration procedure that leverages multiple observations of the same sources over many epochs, to deliver 1%-level photometry across the observed sky.

1. Introduction

LSST aims to deliver 1%-level photometry across the observed sky (0.5%-level for repeat observations of the same source), representing about a factor of two improvement over the current state-of-the-art wide-field optical photometry delivered by SDSS. This factor of two improvement will have a major impact on science deliverables because it implies that the error volume in the five-dimensional LSST color space will be almost two orders of magnitude smaller than for SDSS-like photometry. This smaller error volume will improve source classification and the precision of quantities such as photometric redshifts for galaxies and photometric metallicity for stars.

This factor of two improvement results from two major differences between LSST and SDSS. First, each source will receive hundreds of observations over the ten years of the LSST survey. These series of repeat observations will be used to self-calibrate the photometric system across the sky and for each observation (akin, but not identical to, the uber-calibration procedure used by SDSS (?)), allowing LSST to operate in a wide variety of conditions. Secondly, the wavelength dependence of the hardware and atmospheric transmission response functions will be measured with auxiliary instrumentation on sufficiently fine angular and temporal scales to enable their explicit inclusion in the calibration procedure, rather than resorting to traditional approximations such as linear color terms. CFHT Legacy Survey listed these wavelength-dependent effects as their primary remaining source of error (?).

This document describes the calibration requirements and processes for LSST Data Release photometry. This is a complete recalibration of the data carried out at periodic Data

Release dates, approximately annually (aka Level 2 Data products, in LSST Data Management terms). There will also be a real-time data calibration process, based on the best available set of prior calibrated observations, to provide best-effort precision and accuracy for photometry for quality assurance, generation of alerts, and other quantities appropriate for nightly data generation (aka Level 1 Data Product). The Level 1 photometric calibration is not discussed here.

Section 2 reviews the survey requirements for photometric calibration, while Section 3 describes the philosophy behind LSST’s calibration procedure, first motivating this procedure by describing the true path of a photon through the atmosphere and LSST system and then from the calibration point of view, trying to recreate the transmission of those photons to the focal plane. Section 4 describes details of each step of the calibration procedure, including how each calibration measurement is obtained and applied to the science data along with expected errors originating from each step.

2. Photometric Requirements

The LSST Science Requirements Document (SRD) provides a set of requirements on the annual Data Release (Level 2) photometry based on measurements of bright, unresolved, isolated, non-variable objects from individual LSST visits. Bright implies that the measurement of the star’s brightness is not dominated by photon statistics, approximately 1-4 magnitudes fainter than the saturation limit in a given filter. Isolated implies that the star does not have de-blending problems with background galaxies or nearby stars. Non-variable objects are intrinsically not variable; these will be identified in an iterative fashion from the many epochs of LSST observations. The SRD specifications are:

1. **Repeatability:** the median value of the rms of calibrated magnitude measurements around the mean calibrated magnitude for each star will not exceed 5 millimags in *gri*, 7.5 millimags in *uzy* for bright, unresolved, isolated, non-variable objects. No more than 10% of these objects should have an rms larger than 15 mmag in *gri*, 22.5 mmag in *uzy*. This specifies the distribution of random photometric errors (σ) and constrains both the repeatability of extracting counts from images and the ability to monitor (or model) the changes in normalized system response (ϕ). It could be thought of as making the photometry of a single source consistent over time.
2. **Uniformity:** the rms of the internal photometric zeropoint error (for each visit) will not exceed 10 millimags in *grizy*, 20 millimags in *uzy*, where the zeropoint for each visit is determined using bright, unresolved, isolated, non-variable sources. No more than

10% of these sources should be more than 15 mmag in *gri* or 22.5 mmag in *uzy* from the mean internal zeropoint. This places a constraint on the stability of the photometric system across the sky as well as places an upper limit on various systematic errors, such as any correlation of photometric calibration with varying stellar populations (or colors). This makes the photometry of many sources comparable over the entire sky, which when combined with the previous requirements creates a stable photometric system across the sky and over time, in a single filter.

3. **Band-to-band photometric calibration:** The absolute band-to-band zeropoint calibration for main sequence stars must be known with an rms accuracy of 5 millimags for any color not involving *u* band, 10 millimags for colors constructed with *u* band photometry. This places an upper limit on the systematic error in the measurement of the system throughput as a function of wavelength. This requirement ties photometric measurements in different filters together, enabling colors to be measured for sources with unknown spectral energy distributions (SEDs) or (for sources with known SEDs) magnitudes in different filters to be directly compared.
4. **Absolute photometric calibration:** The LSST photometric system must transform to an external physical scale (*e.g.* AB mags) with an rms accuracy of 10 millimags. This requirement ties LSST internal photometry to a physical scale, and places a constraint on the upper limit of the systematic error in the measurement of the total system throughput. This final step enables LSST photometry to be compared with photometry from other telescopes using other photometric systems.

Requirements 1 and 2 must be met by measuring and then correcting for changes in hardware and atmospheric transmission as a function of time, location in the sky or focal plane, and result in a relative calibration within a single filter. Requirements 3 and 4 require additional measurements of sources with known colors and absolute magnitudes, providing a relative calibration from filter to filter as well as an absolute physical scale for the overall system.

3. Overview of the photometric calibration process

In traditional photometric calibration, a set of standard stars are observed at a range of airmasses to calculate zeropoint offsets and (typically) a single color-dependent extinction term per night. This is sufficient for photometry at the few percent level on photometric nights, however, historical weather data from Cerro Pachon tells us only 53% of the available observing time can be considered photometric even at the 1–2% level. To take advantage

of the full 85% of the available observing time which is usable (total cloud extinction less than 1.5 magnitudes), and to reach the SRD specified requirements – 0.5% level photometric repeatability and 1% photometric uniformity – requires a new approach.

This new approach lies in splitting the measurement of the *normalization* of the throughput in each observation (the gray-scale zeropoint) from the *shape* of the throughput curve (the color dependent terms), and further, using separate procedures to measure the contributions of the telescope hardware response (to the total normalization and bandpass shape) and the atmospheric throughput (to normalization and shape). This allows the use of optimized methods to measure each individual component affecting the final measured magnitudes, allowing us to achieve photometric calibration at the required levels.

A flowchart showing an overview of the steps from science observation to calibrated photometric measurements, together with the required calibration data products is shown in Figure 1. The *normalization* of the throughput will be corrected by using a flat field (for small spatial scale variations) and the self-calibration procedure (for larger spatial scale variations, as this is fundamentally limited by the spacing between calibration stars in each visit). The flat field can only correct for variations in the throughput of the hardware; the self-calibration procedure can correct for variations in throughput due to atmospheric conditions (such as cloud extinction). The *shape* of the throughput curve will be measured using both the narrow band dome screen projector, to correct for variations in the shape of the hardware bandpass response across the field of view, and the auxiliary telescope, to correct for variations in the atmospheric absorption curve from visit to visit.

The rest of this section will provide a more in-depth overview of the calibration measurements required. To motivate the process itself, we will start with a review of what is physically happening to photons in their path toward the focal plane (the ‘truth’). This is then followed by an outline of how LSST will translate the measured ADU counts back to photons above the atmosphere (the ‘model’).

3.1. Truth: From photons to counts

Let us first consider how the photons from an astronomical object are converted into ADUs in the detector, paying attention to the various temporal or spatial scales for variability might arise in the LSST system to affect the final ADU counts. This is the ‘truth’ that the calibration procedure must attempt to recreate, but as the truth, does not include any errors arising from count extraction, measurement of the transmission curves, or zeropoint errors.

Note - while $F_\nu(\lambda, t)$ and other quantities that are functions of time could vary more

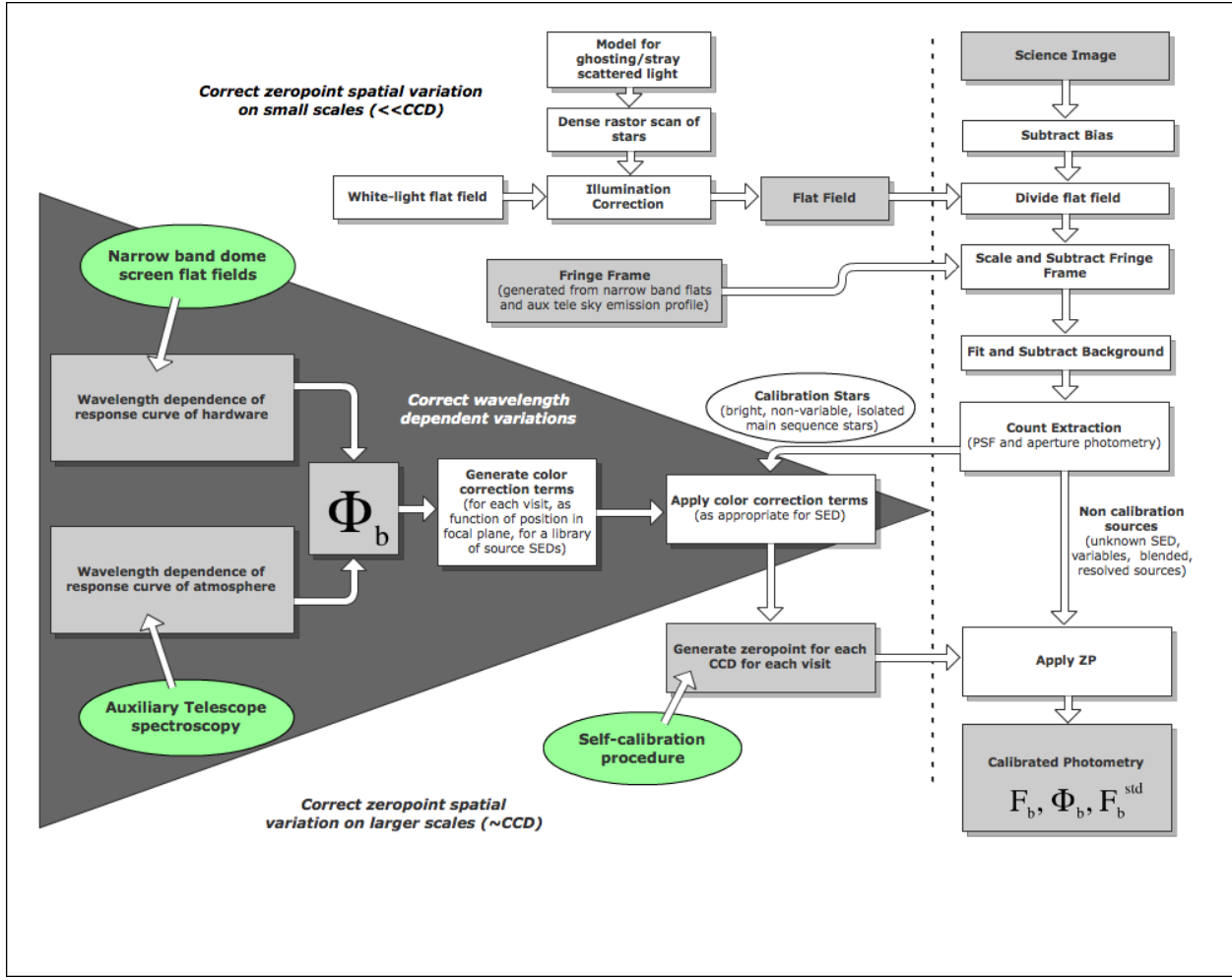


Fig. 1.—: A flowchart of the Data Release photometric calibration process. Everything to the left of the dashed line could be thought of as a calibration product, to be applied to data from each visit on the right of the dashed line. Each of the darker gray boxes indicates data or calibration products required to reach the final goal: calibrated photometric measurements. The light green circles point out significant LSST-specific calibration systems. The separation of the measurement and correction for wavelength dependent (shape) and wavelength independent (normalization) variations in the throughput can be seen in the three sections of the ‘calibration products’ on the left hand side. The upper portion, consisting mainly of flat-field effects, corrects primarily for small spatial scale gray-scale variations (although the illumination correction can have larger spatial scale structure), the middle portion in the dark triangle corrects only for bandpass shape variations, while the bottom portion, consisting of the zeropoint corrections calculated from the self-calibration procedure, will only correct for larger spatial scale variations.

quickly than the standard LSST exposure time of 15s, it is assumed that all such quantities are averaged over that short exposure time, so that t refers to quantities that can vary from exposure to exposure.

Given $F_\nu(\lambda)$, the specific flux of an astronomical object at the top of the atmosphere, at a position described by (alt, az) , the total flux from the object transmitted through the atmosphere to the telescope pupil is

$$F_\nu^{pupil}(\lambda, alt, az, t) = F_\nu(\lambda, t) S^{atm}(\lambda, alt, az, t), \quad (1)$$

where $S^{atm}(\lambda, alt, az)$ is the (dimensionless) probability that a photon of wavelength λ makes it through the atmosphere,

$$S^{atm}(\lambda, alt, az, t) = e^{-\tau^{atm}(\lambda, alt, az, t)}. \quad (2)$$

Here $\tau^{atm}(\lambda, alt, az)$ is the optical depth of the atmospheric layer at wavelength λ towards the position (alt, az) . Observational data (??) show that the various atmospheric components which contribute to absorption (water vapor, aerosol scattering, Rayleigh scattering and molecular absorption) can lead to variations in $S^{atm}(\lambda, t)$ on the order of 10% per hour. Clouds represent an additional gray (non-wavelength dependent) contribution to τ^{atm} that can vary even more rapidly, on the order of 2–10% of the total extinction at 1° scales within minutes (?).

Given the above $F_\nu^{pupil}(\lambda, alt, az, t)$, the total ADU counts transmitted from the object to a footprint within the field of view at (x, y) can be written as

$$C_b(alt, az, x, y, t) = C \int_0^\infty F_\nu^{pupil}(\lambda, alt, az, t) S_b^{sys}(\lambda, x, y, t) \lambda^{-1} d\lambda. \quad (3)$$

Here, $S_b^{sys}(\lambda, x, y, t)$ is the (dimensionless) probability that a photon will pass through the telescope's optical path to be converted into an ADU count, and includes the mirror reflectivity, lens transmission, filter transmision, and detector sensitivity. The term λ^{-1} comes from the conversion of energy per unit frequency into the number of photons per unit wavelength and b refers to a particular filter, *ugrizy*. The dimensional conversion constant C is

$$C = \frac{\pi D^2 \Delta t}{4gh} \quad (4)$$

where D is the effective primary mirror diameter, Δt is the exposure time, g is the gain of the readout electronics (number of photoelectrons per ADU count, a number greater than one), and h is the Planck constant. The wavelength-dependent variations in S_b^{sys} generally change quite slowly in time; over periods of months, the mirror reflectance and filter transmission will

degrade as their coatings age. A more rapidly time-varying wavelength-dependent change in detector sensitivity (particularly at very red wavelengths in the y band) results from temperature changes in the detector, but only on scales equivalent to a CCD or larger. There will also be wavelength-dependent spatial variations in S_b^{sys} due to irregularities in the filter material; these are expected to vary slowly from the center of the field of view to the outer edges, equivalent to a bandpass shift on the order of 1-2% of the effective wavelength of the filter. Wavelength-independent (gray-scale) variations in S_b^{sys} can occur more rapidly, on timescales of a day for variations caused by dust particles on the filter or dewar window, and on spatial scales ranging from the amplifier level, arising from gain changes between amplifiers, down to the pixel level, in the case of pixel-to-pixel detector sensitivity variations.

From equation 3 and the paragraphs above, we can see that the generation of counts $C_b(alt, az, x, y, t)$ from photons is imprinted with many different effects, each with different variability scales over time, space, and wavelength. In particular the wavelength-dependent variability (bandpass shape) is typically much slower in time and space than the gray-scale variations (bandpass normalization). These different scales of variability motivate us to separate the measurement of the normalization of S_b^{sys} and S^{atm} from the measurement of the wavelength-dependent shape of the bandpass.

This then leads us to introduce a ‘normalized bandpass response function’, $\phi_b(\lambda, alt, az, x, y, t)$,

$$\phi_b(\lambda, alt, az, x, y, t) = \frac{S^{atm}(\lambda, alt, az, t) S_b^{sys}(\lambda, x, y, t) \lambda^{-1}}{\int_0^\infty S^{atm}(\lambda, alt, az, t) S_b^{sys}(\lambda, x, y, t) \lambda^{-1} d\lambda}. \quad (5)$$

for each observation. Note that ϕ_b only represents *shape* information about the bandpass, as by definition, $\int_0^\infty \phi_b(\lambda) d\lambda = 1$.

From Equations 1 and 3, we can then recast the counts received from an object as

$$\begin{aligned} C_b(alt, az, x, y, t) &= C \int_0^\infty F_\nu(\lambda, t) S^{atm}(\lambda, alt, az, t) S_b^{sys}(\lambda, x, y, t) \lambda^{-1} d\lambda \\ &= C'^{atm}(alt, az, t) C'_b(x, y, t) \int_0^\infty F_\nu(\lambda, t) \phi_b(\lambda, alt, az, x, y, t) d\lambda \end{aligned} \quad (6)$$

where $C'^{atm}(alt, az, x, y, t)$ and C'_b are wavelength-independent values that depend only on the *normalization* of the independent atmospheric and system throughputs. We can thus measure and apply corrections for the normalization of the atmospheric and hardware transmission separately, without consideration of the shape of the bandpass. We can also introduce a well-defined ‘standard’ bandpass response, $\phi_b^{std}(\lambda)$, chosen during commissioning, so that

$$C_b(alt, az, x, y, t) = C'^{atm}(alt, az, t) C'_b(x, y, t) \times$$

$$\left(\frac{\int_0^\infty f_\nu(\lambda, t) \phi_b^{obs}(\lambda, alt, az, x, y, t) d\lambda}{\int_0^\infty f_\nu(\lambda, t) \phi_b^{std}(\lambda) d\lambda} \right) \times \\ \int_0^\infty F_\nu(\lambda, t) \phi_b^{std}(\lambda) d\lambda \quad (7)$$

where $F_\nu(\lambda, t) = F_o(t) f_\nu(\lambda, t)$, separating the normalization (F_o) and shape (f_ν) of the source spectral energy distribution ($m_{AB} = 2.5 \log_{10}(F_o/3631 \text{ Jy})$). It's worth noting that $\int_0^\infty F_\nu(\lambda, t) \phi_b^{std}(\lambda) d\lambda$ is a constant value for a non-variable source. For convenience, the middle term above can be written as

$$K' \left(\int f_\nu \phi_b^{obs} d\lambda \right) = \left(\frac{\int_0^\infty f_\nu(\lambda, t) \phi_b^{obs}(\lambda, alt, az, x, y, t) d\lambda}{\int_0^\infty f_\nu(\lambda, t) \phi_b^{std}(\lambda) d\lambda} \right) \quad (8)$$

where K' is a value that depends only on the *shape* of the system throughput during a particular observation and the *shape* of the SED of the astronomical object, but does not depend on the normalization of the total throughput or the total flux of the object. Note that K' simplifies to unity if the source SED, $f_\nu(\lambda)$, is constant with wavelength (i.e. a flat SED). The variation in the total counts arising from the K' term is dependent on the cumulative effect of both the atmosphere and the hardware transmission curves on the source SED, thus while the underlying wavelength-dependent (shape) variations in S_b^{sys} and S^{atm} are independent and can be measured separately, the resulting effect can only be applied as a combined correction.

Examples of the effects of variations in the $\phi_b^{sys}(\lambda)$ (hardware response) and $\phi^{atm}(\lambda)$ (atmospheric response) curves on the final observed counts are shown in Figure 2 and Table 1. Two main sequence stellar models (?) – one with temperature 35000K (blue) and one 6000K (red) – were combined with three different atmospheric response curves and two different hardware response curves to illustrate the resulting changes in observed magnitudes. In Figure 3, the $X = 1.5$ atmospheric response is combined with the 1% shift in filter bandpass (altering the hardware response) for many main sequence kurucz models, spanning a range of $g-i$ colors, and the resulting changes in observed magnitudes are plotted. These examples demonstrate that the scatter in observed magnitudes induced by expected atmospheric and hardware transmission curve shape changes alone (without any gray-scale changes) can be larger than the SRD repeatability requirements would permit. Adding variations in the gray-scale normalization due to the hardware response (typically on the order of 0.01 magnitudes) and cloud extinction (could be up to a few magnitudes) will increase the scatter in observed magnitudes.

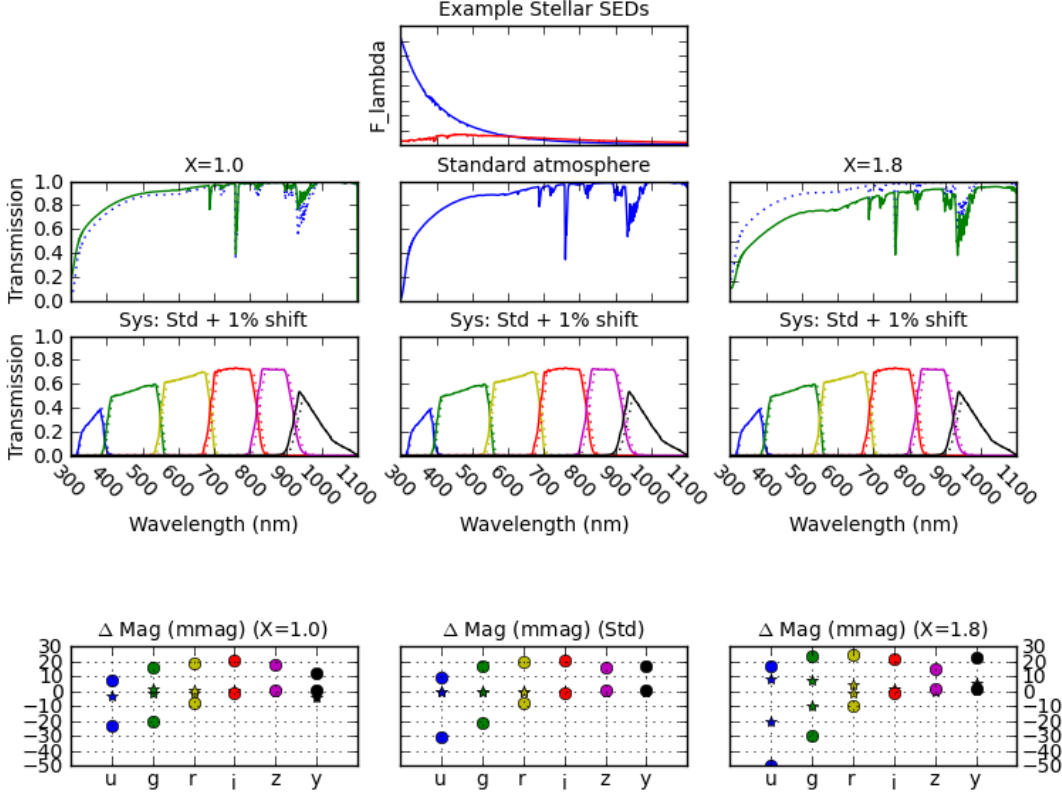


Fig. 2.—: **Changes in observed magnitudes (counts) due to variations in hardware and atmospheric bandpass shape.** Two main sequence kurucz model stars, one blue (35000 K) and one red (6000 K), were used to generate observed magnitudes (equivalent to $-2.5 \log(C_b)$ - the counts in Eqn 7) using three different atmospheric transmission profiles and two different hardware transmission profiles. The stellar flux profiles are shown in the top center panel, while the atmospheric transmission functions ($S^{atm}(\lambda)$) are shown across the second row and the two hardware transmission profiles ($S_b^{sys}(\lambda)$) are duplicated across the third row. The atmospheric transmission profiles correspond to an airmass=1.0, 1.2 and 1.8 (from left to right), with variable atmospheric absorption components. The X=1.0 atmosphere is very similar but not identical to the current LSST default X=1.2 atmosphere throughput curve, which is used as ‘standard’ here. The hardware transmission profiles consist of a ‘standard’ profile (matching the LSST current expected values) and version where the filter throughputs have been shifted by 1% of the effective wavelength of each filter (consistent with the shift expected near the edge of each filter). The final row demonstrates the changes in observed magnitudes produced by the X=1.0, ‘standard’ and X=1.8 atmospheres (left to right, respectively), combined with both the ‘standard’ hardware transmission (represented by the star points) and the +1% shifted hardware transmission (represented by the filled circles) for both the red and blue stars. The exact differences in magnitudes resulting from this calculation are listed in Table 1.

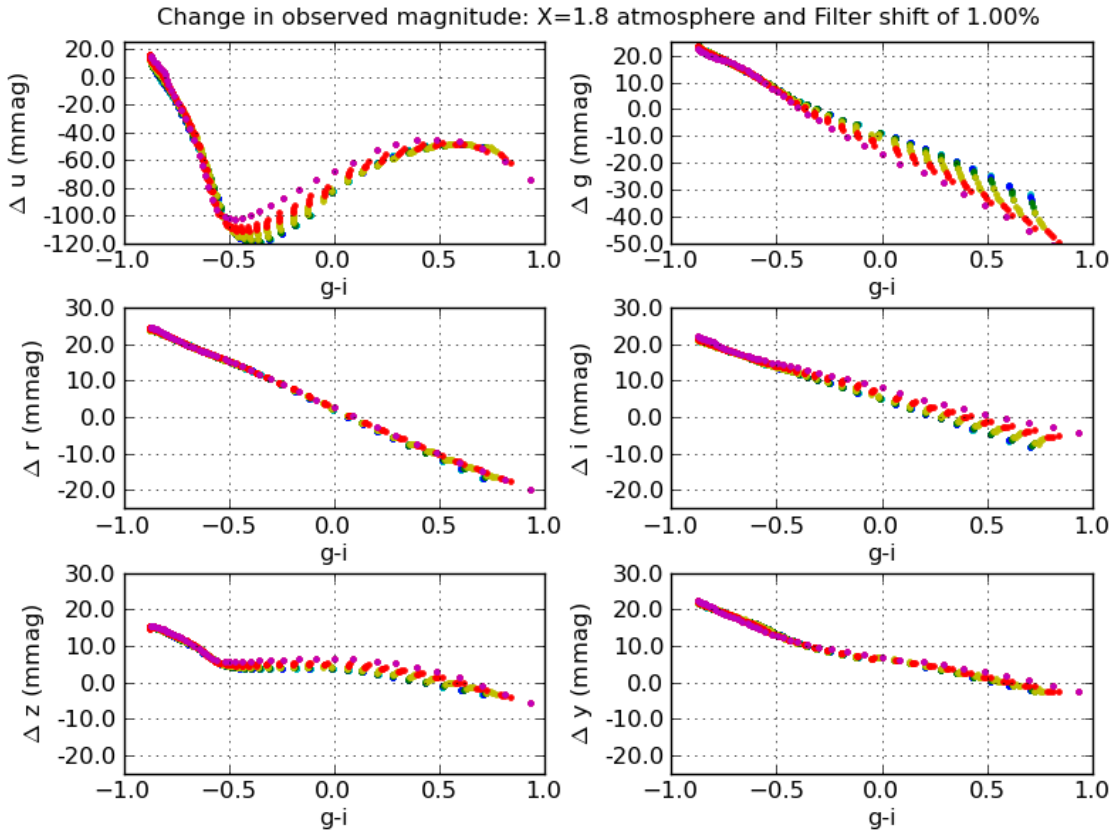


Fig. 3.—: **Changes in observed magnitudes (counts) due to a change in bandpass shape corresponding to a filter shift of 1% and an $X = 1.8$ atmosphere.** 850 Kurucz models with temperatures between 5000K and 35000K and metallicity indexes between -5.0 and 1.0 (solar) were combined with a standard system response (standard atmosphere and standard hardware bandpasses), then with a total system response where the atmosphere was replaced by an $X=1.8$ atmosphere and the filter component of the hardware transmission was shifted by 1% (as in Fig 2). It can be seen that the relationship between Δm and $g - i$ can be parameterized, although generally not with a simple linear relationship. In some cases (such as seen in the Δu and Δg panels), calculating Δm to SRD levels may require more than a simple $g - i$ color, but this is then primarily a function of metallicity which is possible to determine given the $u - g$ color in addition to the $g - i$ information. The points in each plot are color-coded by metallicity, in steps of 1 dex between -5.0 (blue) to 1.0 (magenta).

Table 1:: Changes in observed magnitudes due variations in system and atmospheric bandpass shape (see also Fig 2). The first two rows show the baseline (‘true’) magnitude of the star. All other rows show the *change* in magnitude (in mmag) due to the changes listed at left.

		<i>u</i>	<i>g</i>	<i>r</i>	<i>i</i>	<i>z</i>	<i>y</i>
Standard atm, std sys	red	21.472	20.378	20.000	19.911	19.913	19.913
Standard atm, std sys	blue	19.102	19.503	20.000	20.378	20.672	20.886
Standard atm, +1% sys shift	red	-30.509	-21.591	-8.016	-1.505	0.889	0.944
Standard atm, +1% sys shift	blue	9.480	16.838	19.624	20.462	16.088	16.300
X=1.0, std sys	red	7.470	1.747	0.332	0.045	-0.132	-0.522
X=1.0, std sys	blue	-2.864	-1.319	-0.964	-0.279	0.870	-3.839
X=1.0, +1% sys shift	red	-23.780	-20.165	-7.673	-1.463	0.695	0.451
X=1.0, +1% sys shift	blue	6.966	15.703	18.601	20.249	17.553	12.099
X=1.8, std sys	red	-20.742	-9.581	-1.546	-0.189	0.145	0.634
X=1.8, std sys	blue	7.698	7.515	4.328	1.554	-0.584	5.657
X=1.8, +1% sys shift	red	-49.921	-30.023	-9.531	-1.677	1.088	1.540
X=1.8, +1% sys shift	blue	16.480	23.797	24.042	21.880	14.780	22.326

3.2. From counts to photons

The previous section laid out the origins of ADU count variability from one observation to another. Now we will consider how we can, in practice, acquire the information necessary to convert a particular observed ADU count to a measurement of $F_\nu(\lambda, t)$ above the atmosphere for a particular object. In other words, how we can recreate the ‘truth’ by compensating for the variations in $S^{atm}(\lambda, alt, az, t)$ and $S_b^{sys}(\lambda, x, y, t)$, using the separability of the normalization and shape of the total system response.

Let us first consider measurement of the variations in $S_b^{sys}(\lambda, x, y, t)$. By using a dome-screen system that is capable of producing light at a range of individual wavelengths, we can measure the sensitivity of the hardware (mirrors + lenses + filter + detector) transmission as a function of x, y at each wavelength, producing a data cube of ‘narrow band flat fields’. At a particular x, y location, this data cube records the shape of the transmission response in λ (measuring $\phi_b^{sys}(\lambda, t)$). By flattening the data cube through the λ axis using a chosen spectral energy distribution, the resulting 2-dimensional (x, y) ‘synthetic flat field’ records the normalization of $S_b^{sys}(x, y, t)$. Generation of the synthetic flat field in this manner is time-consuming (requiring many hours to scan through all 6 filters at the necessary wavelength intervals, $\sim 1nm$), however the wavelength-dependent effects are expected to vary only

slowly over time, so the full narrow band flat field scan will only be repeated every 30 days. Since gray-scale normalization changes are likely to occur on a much more rapid timescale, standard white-light flat fields will also be acquired at the start and end of each night. These will be used to correct the normalization of the system response on a nightly basis, updating the synthetic flat field (which has the desired SED) for the current changes in normalization. This flat field correction is particularly important over small spatial scales, as no later calibration stage can contribute to normalization corrections at less than a few times the Point Spread Function (PSF).

It is worth noting that these flat fields (both narrow band and white-light) must themselves be corrected for the effects of pixel scale variations across the field of view, for ghosting caused by internal reflections in the camera and for the presence of stray or scattered light captured in the flat. This correction is called the ‘illumination correction’. The illumination correction will be generated by combining the measurements of the system throughput from the dome screen narrow band flats, measurements of bright, dense star fields rastered across the field of view during specialized observing sequences, and measurements of the ghost patterns at various wavelengths and incident angles obtained with the ‘camera calibration optical bench’ (CCOB). It is likely (as the ghosting pattern is wavelength-dependent) that this illumination correction will have some wavelength dependence. See Figures 5 and 6 for a visual example of the illumination correction and effect on image processing. The illumination correction is expected to be stable with time and will be remeasured only when the optical path of the telescope is altered.

Next, considering $S^{atm}(\lambda, alt, az, t)$, we will again separate the measurement of the shape of the atmospheric response and the measurement of normalization of the transmission. The wavelength-dependent variations in $\phi^{sys}(\lambda, t)$ change smoothly over spatial scales larger than the field of view and over several minutes. By using an auxiliary telescope equipped with a spectroscope to observe bright stars with known SEDs, we can measure atmospheric absorption at a variety of positions in the sky every 5–10 minutes throughout the night. These observations are used as constraints for MODTRAN atmospheric models, generating simpler representations of the atmospheric throughput (in the form of a set of absorption components as a function of alt, az, t). These components can be interpolated to generate a wavelength-dependent atmospheric absorption profile, $S^{atm}(\lambda, alt, az, t)$, for each observation. In order to correct for the higher frequency gray-scale variations in the normalization of $S^{atm}(alt, az, t)$ due to cloud extinction, we must use the observations of stars in the images themselves, as the cloud extinction can vary up to 0.01 magnitudes on the scale of a CCD (?) as fast as a few minutes. This ‘self-calibration’ procedure could be thought of as creating a massive calibration ‘standard’ star catalog, where the calibration stars are all of the non-variable, main-sequence stars in the science images; the main difference is that the true magnitudes

of the calibration stars have to be bootstrapped from the many different observations of the survey. The calculation of the calibration star magnitudes and the determination of the normalization for $S^{atm}(alt, az, t)$ are achieved simultaneously. First the previously described corrections for $\phi^{atm}(\lambda, t)$, $\phi_b^{sys}(\lambda, t)$ and the flat field normalization must be added to each observation, producing a ‘standardized’ magnitude for each star, and then in ‘self-calibration’, we minimize the difference between the standardized magnitude and a model magnitude,

$$\chi^2 = \sum_{ij} \left(\frac{m_{b,ij}^{std} - m_{b,ij}^{model}}{\sigma_{b,ij}^{std}} \right)^2 \quad (9)$$

where the model magnitude is derived from the best-fit ‘true’ magnitude of the calibration star and the normalization constant (zeropoint offset) for this ‘patch’ (equivalent to the size of a CCD)

$$m_{b,ij}^{model} = m_{b,i}^{best} - \delta z_{b,j}. \quad (10)$$

This produces best-fit magnitudes for the calibration star catalog as well as zeropoint offsets (normalization constants) for each CCD in every observation. This procedure can also correct for variations in the normalization of the total system throughput beyond those contributed by cloud extinction, but will not be sensitive to changes on scales smaller than a patch. This is similar in nature to the ubercal method applied to SDSS in ?.

Using Equation 7, we can define a ‘natural magnitude’

$$m_{nat} = -2.5 \log_{10} \left(\int_0^\infty F_\nu(\lambda, t) \phi_b^{std}(\lambda) d\lambda \right) \quad (11)$$

$$= -2.5 \log_{10} \left(\frac{C_b(alt, az, x, y, t)}{C'^{atm}(alt, az, t) C'^{sys}_b(x, y, t) K'(\int f_\nu \phi_b^{obs} d\lambda)} \right) \quad (12)$$

describing the quantity we wish to derive from the measured ADU counts. The natural magnitudes can be related to the corrections just described above by

$$\begin{aligned} m_b^{nat} &= -2.5 \log_{10} (C_{b,raw}(alt, az, x, y, t)) \\ &\quad + \delta z_b^{ff}(x, y, t) + \delta z_b^{selfcalib}(alt, az, t) \\ &\quad + \delta k_b^{atm+sys}(alt, az, x, y, SED, t), \end{aligned} \quad (13)$$

where δz_b^{ff} comes from the normalization constant derived from the illumination-corrected synthetic flat field, updated for variations in normalization on a night-to-night basis by the white-light flat (and applied directly to the science images at the pixel level in the traditional manner), $\delta z_b^{selfcalib}$ comes from the normalization constant derived from the self-calibration method, and $\delta k_b^{atm+sys}$ depends on the shape of the total system response (atmosphere +

hardware measured from the auxiliary telescope and the narrow band flat fields) as well as the shape of the source SED. The color-term correction $\delta k_b^{atm+sys}$ is effectively a lookup table for each observation, where $\phi_b^{sys}(\lambda, x, y, t)$ and $\phi^{atm}(\lambda, alt, az, t)$ are combined with a series of model SEDs and the resulting magnitude variation is recorded as a function of source SED and x, y in the focal plane (as the atmospheric variation is roughly constant across the field of view). For many sources (but not calibration stars) LSST will simply assume a flat SED, at which point the $\delta k_b^{atm+sys}$ correction becomes zero, and users may create their own SED and correction tables based on their knowledge of the true SED (see Appendix ??).

These natural magnitudes are calibrated for variations in the observed bandpass shape (where applicable) and normalization, thus are directly comparable from one observation to another. However, they are not tied to an external physical scale (or from one filter to another), and thus only define an internally calibrated LSST magnitude in a particular filter.

To fulfill SRD requirements 3 and 4, these internally calibrated natural magnitudes must be tied from one filter band to another, and then tied to an absolute external physical scale. For this, a further set of measurements is needed. In all filters, a set of objects with a well-known spectral type (such as main sequence stars or white dwarfs, preferably with direct observations of the SED of the specific object) must be observed and calibrated, in individual filters, as above. The prior knowledge of each SED is combined with the standard bandpass shape to generate synthetic color photometry. These synthetic colors are then compared with the calibrated measured natural magnitudes to calculate Δ_{b-r} , the corrections needed to tie measurements in each filter together (referenced to r band). At this point, only one final measurement is necessary to tie the entire system to an external physical scale: an r band LSST natural magnitude measurement of an absolutely calibrated source on a photometric night. Although in theory these last two steps could be done with a single externally calibrated object, on a single photometric night, a larger set of external reference objects with well known AB magnitudes will be used to reduce systematic errors. This defines an AB magnitude,

$$m_b^{AB} = m_b^{nat} + \Delta_{b-r} + \Delta_r \quad (14)$$

which can be compared to absolute physical flux scales.

The sequence for photometric calibration is then:

1. Acquire narrow band flat fields on a monthly basis, acquire white-light flat fields to update the narrow band flat fields on a nightly basis, and generate an illumination correction on a many-monthly basis. Apply the illumination correction to the narrow band flat fields and combine the narrow band flat fields into a synthetic flat using

a chosen SED (perhaps mimicking the night sky SED). Scale the synthetic flat for any measured changes in the white-light flat occurring since the generation of the synthetic flat. Apply final synthetic flat to images directly, dividing science images by the synthetic flat field.

2. After remaining image processing (bias correction, fringe correction, etc) extract ADU counts of sources from images.
3. Acquire spectra of known stars on a 5–10 minute timeline throughout each night, fit for atmospheric absorption coefficients and generate atmospheric response curve for each science image’s alt, az, t based on MODTRAN models, retrieve hardware response curve from narrow band flat fields at various x, y locations within the focal plane. Using a range of model SEDS, generate a table of $k_b^{atm+sys}(x, y, SED)$ corrections for each observation. Apply $k_b^{atm+sys}$ corrections to stars chosen for self-calibration.
4. At appropriate intervals (such as at Data Release), minimize χ^2 from Equation 9 for the self-calibration stars and record $\delta z_b^{selfcalib}$ for each patch (each CCD in each observation).
5. Apply $\delta z_b^{selfcalib}$ to all stars in calibration patch. If an SED is known or has been chosen for particular science targets, apply appropriate $k_b^{atm+sys}$ correction.
6. Apply measured corrections Δ_{b-r} and Δ_r .

resulting in calibrated m_b^{AB} values in a standardized bandpass shape, with above-the-atmosphere fluxes.

4. The internal calibration process

The next subsections expand on each of the internal calibration steps leading to natural magnitude measurements described above, including how each correction is measured, calculated and applied. These steps described in this section are applied to each filter independently. The end result of the internal calibration process is a set of natural magnitudes, m_b^{nat} , measured for each object in each visit, together with a record of $\phi_b^{sys}(\lambda, x, y, t)$ and $\phi^{atm}(\lambda, alt, az, t)$ (the shape of S_b^{sys} and S^{atm}), the flat field applied (normalization of S_b^{sys}), the zeropoint offset calculated for cloud extinction (normalization of S^{atm}) and the spectral energy distribution assumed for the object to calculate m_b^{nat} (which may be a flat SED, in which case m_b^{nat} only includes normalization corrections).

4.1. Normalization of the hardware transmission

Compensation for variations (in x, y, t) in the normalization of the hardware transmission (S_b^{sys}) will be done using a flat field measured using narrow band and white light flat fields, after these are corrected for differences in illumination patterns between the dome screen and the night sky (the ‘illumination correction’). This is the first step in photometric calibration and is necessary to correct for variations in the normalization of S_b^{sys} that are smaller than a few times the PSF (and in the current calibration implementation, smaller than the scale of a CCD).

The specialized hardware for this flat field measurement is an array of projectors mounted in the dome of the LSST enclosure instead of the traditional ‘dome screen’. These projectors will be illuminated with both broadband (e.g. quartz lamp) and tunable narrow band (essentially monochromatic) light sources. Adjustment of the wavelength of the tuneable narrow band light source can be as fine as 1 nm. The projectors are designed to fill the LSST etendue with a uniform illumination, smoothly varying by less than 1% across the camera field of view (corresponding to less than 10% variability across the projector surface) and less than 0.25% on scales smaller than 0.5° (a little larger than the size of a CCD). The projectors will also be designed to limit the extent of light emitted outside the range of angles seen by the camera to reduce stray light in the flat fields (?). A set of precision diodes will be used to normalize the photon flux integrated during flat field exposures, thus allowing a precise comparison of the system response at different wavelengths when using the narrow band light sources. These photodiodes, together with their read-out electronics, will be calibrated at the U.S. National Institute of Standards (NIST) to $\approx 0.1\%$ relative accuracy across wavelengths from 450 nm to 950 nm. The response of these diodes varies smoothly across this range of wavelength and provides a well-behaved reference for determination of $S_b^{sys}(\lambda)$. Further details of the LSST narrow band flat field apparatus can be found in ?. Preliminary results from a similar apparatus tested at PanSTARRS can be found in ?, as well as earlier experiments from CTIO described in ?.

In each filter, a set of narrow band flats will taken at a series of wavelengths to form a data cube of flat fields in (x, y, λ) . Using the photodiode measurements of the light emitted at each wavelength, the data cube can be collapsed to a single ‘synthetic flat field’ image (x, y) by choosing a desired spectral energy distribution, then combining the individual narrow band images after applying an appropriate illumination correction (see subsection 4.1.1 for details on the illumination correction) for each wavelength and weighting by the goal SED and the photodiode measurements. The desired SED could be a single, constant SED or could be a set of SEDS, but will be clearly defined during the commissioning period. One choice might be a night sky SED to match the majority of pixels in each image; the goal

SED would then vary throughout the lunar cycle.

The narrow band flats are time-consuming to acquire. Scanning through all 6 filters at 1 nm intervals requires many hours worth of exposures, but must also be done in minimal levels of ambient light. Luckily, any wavelength dependent variations in the synthetic flat are expected to change relatively slowly so the full set of narrow band flats only need to be acquired approximately once a month, which could be done during cloudy nights. However, gray-scale variations in the hardware normalization (due to dust particles on the filters, etc.) will occur on a much shorter timescale. Thus, it is necessary to use a standard white-light flat to correct for these short timescale gray-scale variations in the system throughput. The white-light flat fields will be obtained with the same apparatus as the narrow band dome flats, but as the number of exposures required to characterize a filter is dramatically reduced, these white-light flats can be obtained at the start and end of every night of observing.

The white-light flat is not applied directly to images, as it does not have the desired spectral energy distribution. Instead, changes in the white-light flat from night to night will be transferred to the data cube of narrow band flat fields, adjusting the narrow band flats for small-scale changes in gray-scale throughput. This can be done by taking a white-light flat simultaneously with the acquisition of the narrow band flat data cube. White-light flats obtained over the next month are compared to the ‘simultaneous’ white-light flat, and then the narrow band flat data cube can be multiplied by any observed differences.

The illumination pattern and color of the quartz lamp must be stable over the time interval between monthly narrow band flat measurements, to reduce changes in ghosting or color-dependent sensitivity variations in the white light flats.

4.1.1. Generating the illumination correction

The ideal flat field would demonstrate the hardware response to a focal plane illuminated exactly as it would be with a dark night sky, empty of ghosts, glints, stray or scattered light - recreating the hardware sensitivity variations across the focal plane as well as the effects of vignetting, both of which must be accounted for in the science images. The measured flat field, however, not only contains the actual vignetting and hardware sensitivity variations but also variations in the actual illumination pattern of the dome screen projectors, stray light, ghost images of the dome screen, and the effect of pixel scale variations across the field of view, which must be removed using the illumination correction.

The dome screen projectors will be designed to be uniformly illuminated to 1% over the focal plane, but this is already beyond the SRD specifications for photometric uniformity.

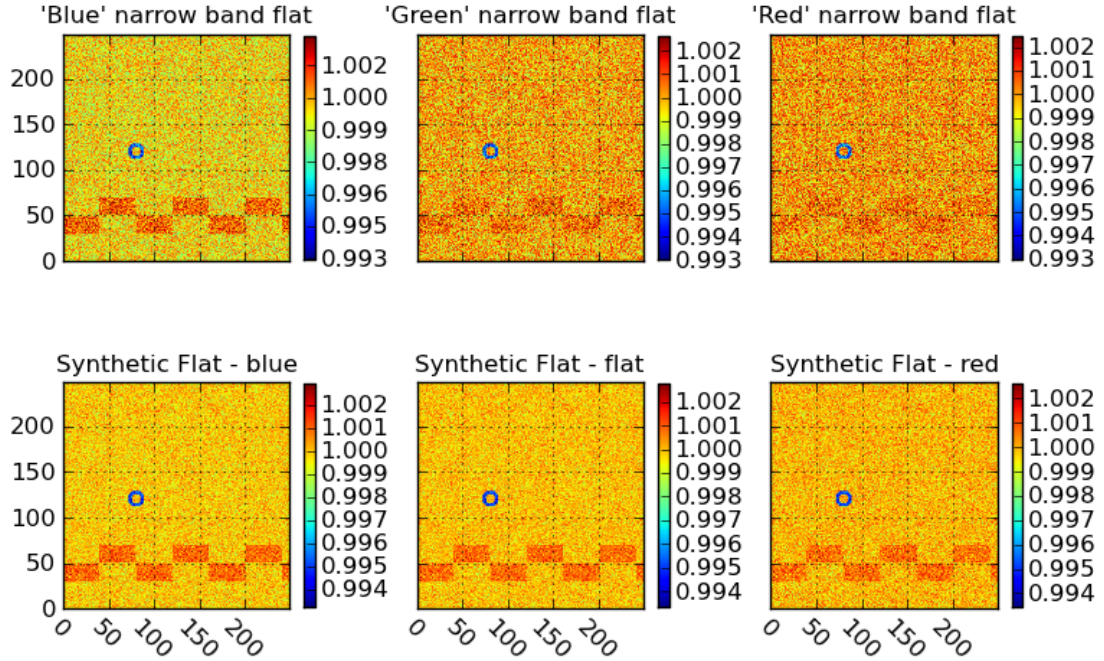


Fig. 4.—: **Simplified examples of synthetic flat generation.** The top panel illustrates simplified narrow band flats, at 'blue', 'green' and 'red' wavelengths. These represent illumination corrected (thus the relatively flat illumination pattern!) narrow band flat fields, where the detector shows a sensitivity pattern that is more pronounced in the blue wavelength flat field. The bottom panel shows the result of combining these flats to create a synthetic flat with a desired SED that is either weighted toward blue wavelengths ($1.5 \times \text{blue} + 1.0 \times \text{green} + 0.5 \times \text{red}$), a completely even distribution, or a synthetic flat weighted toward red wavelengths ($0.5 \times \text{blue} + 1.0 \times \text{green} + 1.5 \times \text{red}$). In operations, the synthetic flat will be created using a well-defined SED that will best correct the system normalization for science targets in the field.

There will be also light scattered within the camera dewar and some fraction of the light within the etendue will have undergone multiple reflections within the camera refractive optics (creating ‘ghost’ images of the light from the dome screen). Estimates by Photon Engineering, Inc. (Tucson, AZ) indicate that $\approx 1 - 2\%$ of the light that reaches the camera focal plane may be stray light that did not originate within the LSST etendue. In addition, projection effects cause a variation in the pixel scale from the center to the outer edges of the field of view, so that the pixels subtending a larger area (the center of the field) gather more light from the dome screen. This effect *is* present in the night sky science images as well, but does not affect the total flux measured from astronomical objects, so this gradient must be preserved in the science images (and thus removed from the flat field through the illumination correction).

Illustrative examples of these effects in a theoretical dome flat and the corresponding illumination correction are shown in Figure 5, and the effect of this illumination correct on final measured counts are shown in Figure 6.

Illumination corrections (one per filter) will be generated whenever the camera is removed from the telescope or the focal path undergoes significant changes (such as a filter being replaced or the mirrors being realuminized), but should be stable otherwise. The corrections will be created by combining information from a ZEMAX model of ghosting in the camera constrained by measurements from the Camera Calibration Optical Bench (CCOB), measurements of the observed individual narrow band dome screen (DS) flats, and dense star fields restored across the focal plane on a photometric night.

The first of these components, **Camera Calibration Optical Bench (CCOB)**, provides a method to calibrate the spatial and wavelength-dependent response of the focal plane, unmounted from the telescope, using a well controlled, wavelength-variable, light source calibrated using a NIST photodiode. This light source, which produces a spot in the focal plane approximately the size of or smaller than the PSF, will be scanned across the detector (x, y) at a variety of beam incident angles, (θ, ϕ) and at a variety of wavelengths (λ). The response of the detector will be measured in two different configurations: one with only the detector and the dewar window - which doubles as lens 3 (L3) - and one with the detector, L3, L2, L1, the filters and the camera shutter. In the L3-only configuration, the detector response should include only relative simple ghosting, primarily 3 ghost images from reflections between the CCD surface and L3. In the full refractive optics configuration (with L3, L2, L1, the filter and camera shutter), the detector response will include a more complicated ghost pattern. Current simulations indicate the strongest ghosts are expected to originate from reflections between the CCD surface and L3, where the resulting ghosts are expected to have an amplitude $5 \times \approx 10^{-4}$ relative to the flux of the source. Other ghost images,

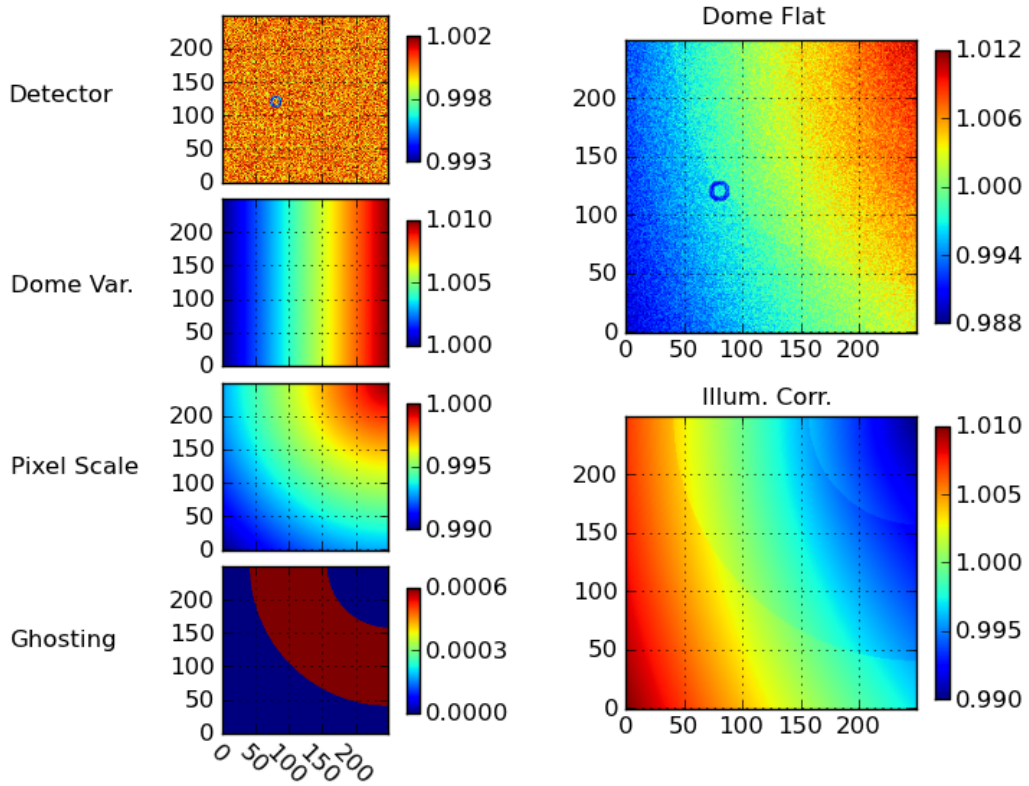


Fig. 5.—: **Components of the illumination correction.** Any flat field obtained from the dome screen includes not only a measurement of small-scale variations in detector sensitivity (Detector panel, top left), but also records unwanted effects such as variations in the dome screen illumination as a function of position (Dome Var. panel), variations in brightness that result from variations in the amount of sky observed by each pixel (arising from variations in the pixel scale over the focal plane) (Pixel Scale panel), and ghosting caused by internal reflections in the camera (Ghosting panel). Each panel on the left demonstrates the effect on the total flat field attributable to each of these variations, in a simplified manner. Variations are generated as follows: pixel-to-pixel variation in detector sensitivity is 0.4% (as well as a small dust ring), the dome screen has a 1% gradient across the field of view, the pixel scale changes by 0.5% from corner to corner, and the ghosting is generated by adding 0.1% of the total light into a ring reflection. The top large panel on the right shows the dome screen flat field that would be observed after combining all of the effects on the left. The bottom large panel on the right shows the illumination correction that must be multiplied with this flat field to remove the effects of the dome screen variation, the pixel scale variation, and the ghosting. Note that no photon noise was introduced in this simulation.

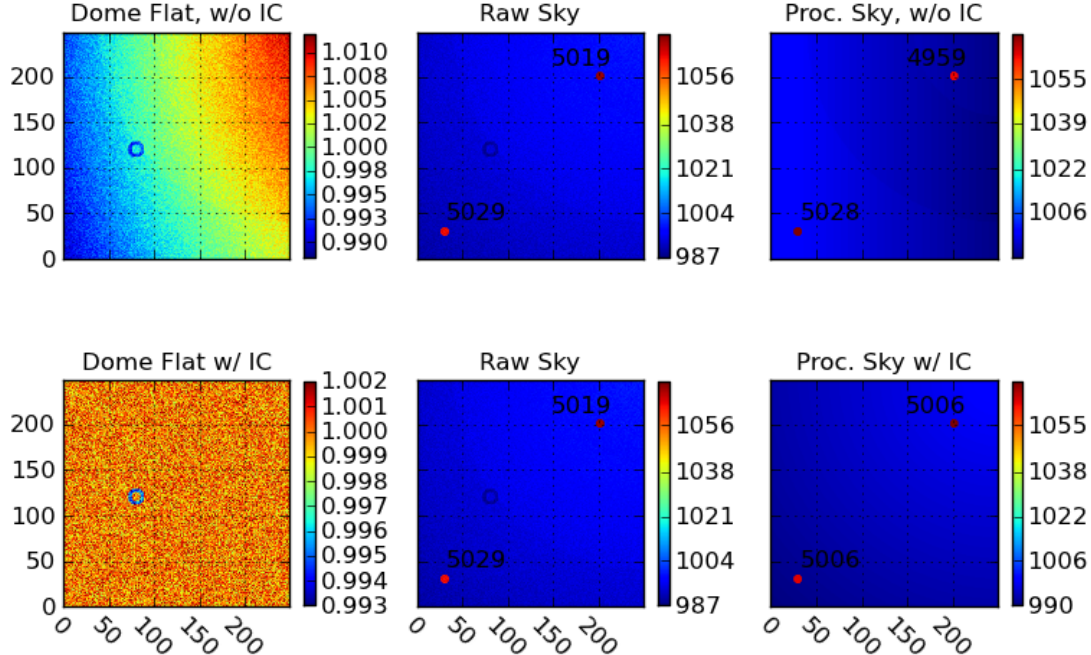


Fig. 6.—: **Effect of illumination correction on photometry.** The left top panel shows a flat field obtained from a dome screen, creating with the same conditions as in Figure 5, without multiplying by an illumination correction. The central top panel shows a raw ‘image’ of the sky, generated by adding a background sky value of 1500 counts per pixel (scaled by the pixel area, as in Fig. 5, to two stars. The stars were generated by placing 5000 counts over a circular aperture the size of the PSF at the location of the star. A ghost image was created as in Fig. 5. The right top panel demonstrates the result of processing the raw sky image by subtracting the ghost image and then dividing by the dome flat without an illumination correction. The left bottom panel shows the illumination correction applied to the same flat field. The middle bottom panel shows the same raw sky image as the top row. The bottom right panel demonstrates an improved processing of the raw sky image, by subtracting the ghost image and then dividing by the illumination corrected flat field. Note that the sky background does not appear flat but is correct for preserving stellar photometric accuracy. In every image with stars, the numbers next to each star indicate the counts measured within an appropriate circular aperture for the star. In the raw images, these counts are not equal because of the variation in pixel to pixel sensitivities.

due to reflections between lens surfaces, should contain about $\approx 10^{-5}$ times the flux of the source. See Figure 7 for an example of simulated ghosting in the LSST focal plane. These measurements of the focal plane response in different optical configurations with a known incoming light source do not directly measure the illumination correction (for example, neither pixel scale variation due to projection effects nor the full stray/scattered light from the dome projectors are included), but it does provide constraints for model calculations (such as a ZEMAX model) of the illumination pattern in the camera as a function of wavelength, position in the focal plane, and beam incident angles, which are necessary for the creation of the full illumination correction, as well as constrain the focal plane response itself.

More details about the requirements and physical apparatus of the CCOB are available in LSST-10015 and LSST-8217.

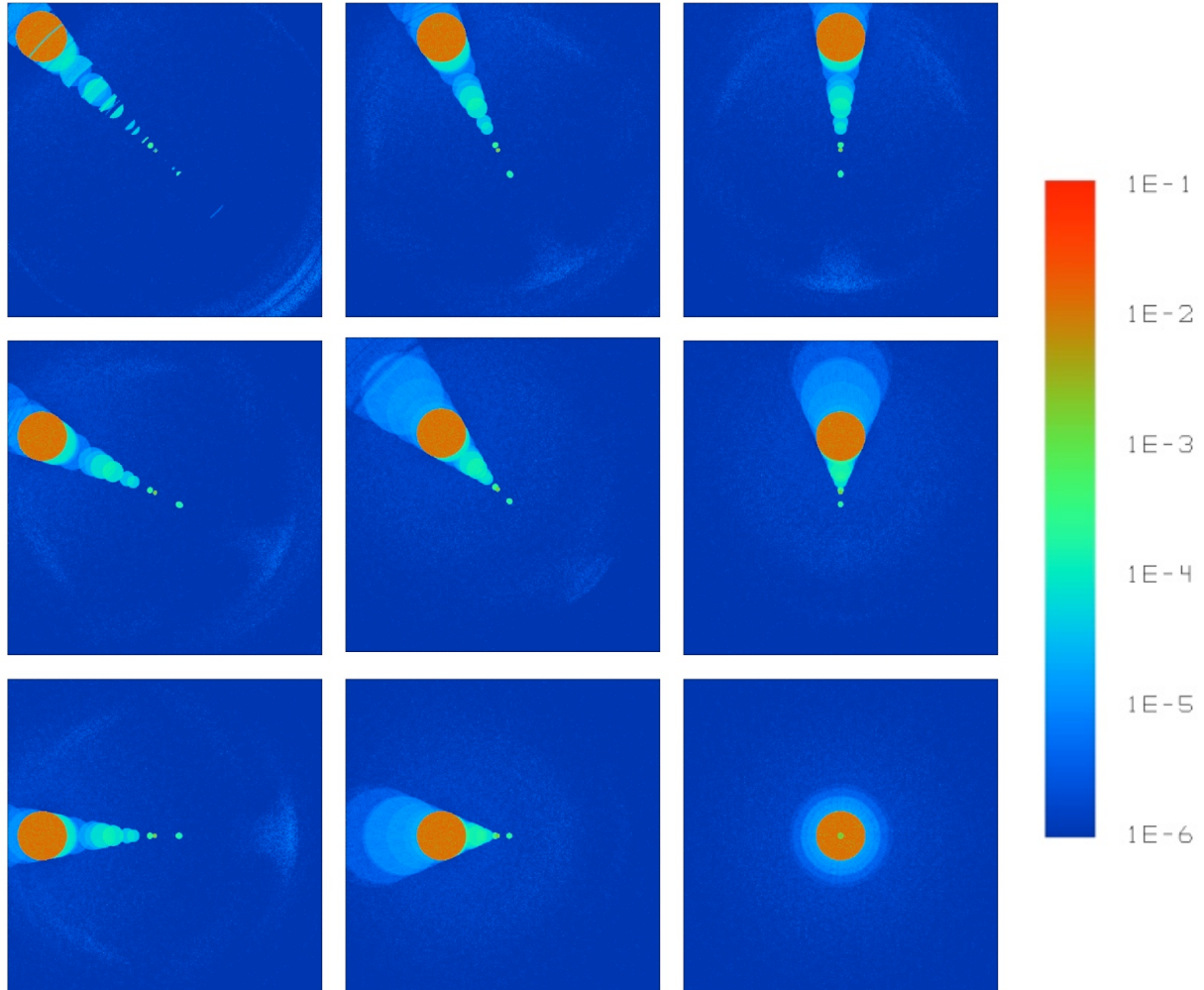
The ZEMAX model describes how light scatters inside the camera creating ghosts at each wavelength. If the dome screen projectors were perfectly uniform and no stray light was scattered into the LSST etendue, the narrow band dome flats plus the predictions from the ZEMAX model would suffice to create a perfect illumination corrected synthetic flat. Stray light scattered into the LSST etendue can be modeled using work similar to that of Photon Engineering, Inc., and then the model constrained by taking measurements of the focal plane response while blacking out M2 (to image only the stray light). This creates a preliminary estimate of the illumination correction, which is particularly useful for small spatial scales (smaller than a CCD) which may not be well sampled in the next, raster-scan step.

To account for illumination variations from the dome screen projectors on large spatial scales (which could be up to 1% across the field of view), stray light scattered from other unmodeled surfaces, or systematic differences in exposure time due to the camera shutter movement, a dense network of stars of a variety of spectral types must be rastored across the focal plane on a photometric night. The images will be divided by the synthetic flat field corrected by the preliminary illumination correction, and then the counts for each star corrected for varying color terms in the atmosphere and hardware response, as further described in subsection 4.2. The final update to the illumination correction can then be determined by minimizing over all stars i in all observations j ,

$$\chi^2 = \sum_{i=N_{stars}, j=N_{obs}} \left(\frac{m_{ij}^{meas}(x, y) - m_{ij}^{model}(x, y)}{\sigma_b} \right)^2 \quad (15)$$

where the model magnitude of each star in each observation is given by

$$m_{ij}^{model}(x, y) = m_b, i^{best} - \delta k_{b,j}^{atm+sys}(x, y, alt, az, SED, t) - \int d\lambda dZ_{IC}(x, y, \lambda) \quad (16)$$



K. Bechtol (SLAC/KIPAC). Image from LSST Document 10008.

Fig. 7.—: **Simulations of LSST camera ghost images, as measured by CCOB.** Various beam incident angles, positions and wavelengths will be explored by the CCOB, creating focal plane measurements similar to those simulated above. These measurements will be combined to constrain a ZEMAX model describing the optical paths in the camera (including the effect of the actual coating reflectivities of the CCD and lens surfaces, etc).

where $m_{b,i}^{best}$ is the best-fit, constant magnitude of the star in this filter, $k_{b,j}^{atm+sys}$ is the color-term correction (partially determined by the constant from exposure-to-exposure hardware throughput curve and partially determined by the varying with each exposure atmospheric throughput curve), and dZ_{IC} is the update to the illumination correction which is produced by this dense rastor scan. Similar applications of rastor scans have been successfully used in previous surveys, (*e.g* ???), providing an illumination correction accurate to the sub-percent level. With the additional information from the CCOB and the better intrinsic uniformity of the dome screen illumination, we expect the illumination correction for LSST to be at least factor of 2 more accurate.

4.1.2. Error in the Normalization of the Hardware Transmission

The dome screen projectors will be designed to be uniform to better than 0.25% (2.5 mmag) over scales less than 0.5° (slightly larger than a CCD). Translating from this engineering requirement (a strict limit) to the RMS of expected measurements implies a resulting RMS of 0.7 mmag ($=2.5 \text{ mmag}/\sqrt{12}$) in the dome illumination uniformity on scales smaller than a CCD. After using the measurements from the CCOB to model ghost reflections and scattering within the camera, the uniformity of the dome screen projectors is expected to be the limiting factor on these small scales. Applying the dense rastor scan of stars to correct for larger illumination variations from the dome screen projectors on the scale of the entire field of view, plus to correct for the effects of 1–2% stray light and systematic exposure differences due to camera shutter travel, adds an additional error of about 2.8 mmag, increasing the expected error in the illumination corrected synthetic flat field to 2.9 mmag.

The illumination corrected synthetic flats are created on a monthly basis and then must be updated for gray-scale nightly changes in the hardware transmission (due to dust,etc) using the white-light flat fields acquired using the quartz lamp in the dome screen projectors. As this update only depends on changes in the white light flats, not their absolute values, the only requirement is that the quartz lamps produce an illumination pattern in the focal plane which is stable over time at the same level as the initial illumination uniformity requirement, or stable to within 0.25% within a CCD. This means that the quartz lamps should not change their spectral profile (which may change the ghosting pattern due to wavelength dependent effects) or their illumination pattern by more than an amount which would produce changes of more than 0.25% in the focal plane, adding a further 0.7 mmag rms scatter, for a final total of 3 mmag expected error in the normalization of the hardware throughput.

4.2. Shape of the Hardware and Atmospheric Response

Compensation for the changes in observed magnitudes caused by variations in the wavelength dependence (shape) of the hardware and atmospheric response curves, $\phi_b^{sys}(\lambda)$ and $\phi^{atm}(\lambda)$, will be done using independent measurements of the hardware response curve (from the narrow band flat fields) and the atmospheric response curve (from atmospheric extinction models generated from measurements from the auxiliary telescope). While the measurement of the shapes of the hardware and atmosphere curves are independent, the actual correction that must be applied depends on the combination of atmospheric and hardware response curves as well as the SED of the astronomical object. This correction is necessary for precision photometry, but as it requires knowledge of the object’s SED, most LSST reported magnitudes will include either no correction or a (potentially rough) correction along with an indication of what SED was assumed to generate this value. However, for stars which will be used in self-calibration (see subsection ??) to determine photometric zeropoints in each exposure, a model SED well-matched to the object’s colors will be chosen and used to generate the $\delta k_b^{atm+sys}$ corrections described in this section.

It is worth emphasizing as we start this section that $\delta k_b^{atm+sys}$ is a correction for changes in the *shape* of the bandpass only; any grayscale components to the changes in bandpass shape discussed here are not part of $\delta k_b^{atm+sys}$ and instead belong to either the hardware or atmospheric *normalization* corrections.

4.2.1. Measuring the shape of the hardware response curve

The hardware response curve is measured directly using the individual narrowband flat fields described in section 4.1. At each wavelength, the narrowband flat field will be illumination corrected and then used to measure the total hardware response over all x, y positions. The dome screen photodiodes will be used to track the relative intensity of the light produced by the projectors at each wavelength. These NIST-calibrated photodiodes are expected to be accurate to within 0.1% between 400-900 nm (g, r, i, z bandpasses) with current technology, which can be extended to 1600 nm (into the y band) using techniques under development (which also have the possibility of achieving 0.01% accuracy in the diode calibration at NIST) (?), as shown in Figure 8.

These measurements will be updated on a monthly basis, as the hardware response curve is expected to change only slowly over time due to aging in the filter and mirror coatings. It is expected that the shape of the response curve will be primarily a function of radius due to variations in the thickness of the filter coatings caused by the mechanism used to deposit

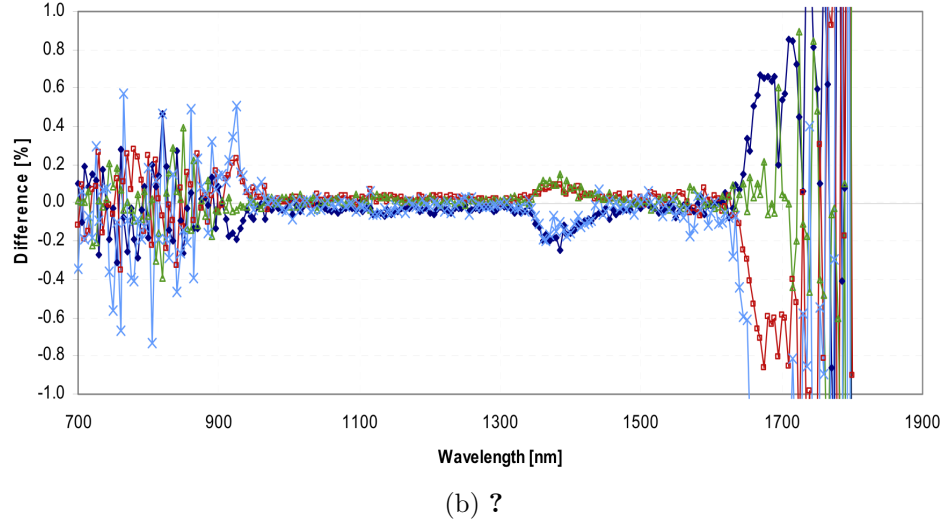
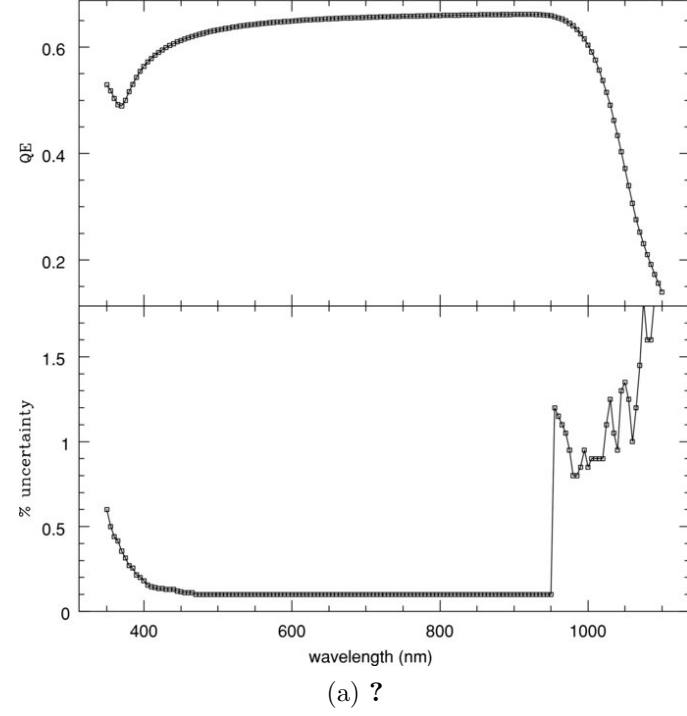


Fig. 8.—: **Quantum efficiency curve and fractional uncertainty for NIST-calibrated photodiode, from ? and ?.** Panel (a): Between 400 and 900 nm, calibration methods already in use in test systems indicate photodiode accuracy is better than 0.1%, as in the bottom part of this panel. The sudden decrease in calibration accuracy below 900 nm is due to calibration methods used by NIST in 2005. Panel (b): More recent photodiode calibration efforts by ? show better than 0.1% accuracy can be achieved to beyond 1200 nm, the limit of detector response for LSST, as shown here in the response curves resulting from multiple scans of a single source using the same photodiode.

those coatings. The variation due to filter nonuniformities is specified to be less than 1% across the focal plane, most likely in the form of a bandpass shift as shown in Figure 9. For main sequence stars, the resulting changes in observed magnitude as the bandpass shifts by 1% of the central wavelength can be as much or more than 0.04 magnitudes (40 mmag) – even larger in the u band (see Figure 10). However, as long as the variation in the hardware response curve is measured to better than 0.05% – equivalent to approximately a 3 Angstrom error in wavelength calibration of the monochromatic light source throughout the bandpass or a 0.5% error in photodiode calibration assuming that the shape of each bandpass is determined using at least 100 independent measurements (i.e. 1 measurement every few nanometers within the bandpass) – the maximum error contribution towards calibrating these observed magnitudes will be less than 2 mmag for all bandpasses other than u , where the error could be as much as 5 mmag for certain main sequence stars (see Figure 11).

Because the shape of the hardware response curve varies as a function of filter radius, it is also necessary to monitor any offsets of the filter position from dead center after any filter changes. Assuming the filter response curve varies linearly with radius, the filter location must be measured to better than 0.025% for the filter positioning to remain less than a 1 mmag source of error.

LJ - beamsize 100mm, plus review filter location requirement ... 0.025Plus need to include shift in bandpass due to change in incident angle ?

4.2.2. Measuring the shape of the atmospheric transmission curve

The atmospheric transmission curve appropriate for each observation will be generated using data from spectroscopic measurements of bright stars obtained with the LSST auxiliary telescope, which is fit to an atmospheric extinction model to determine the atmospheric transmission profile at all points on the sky at all times. This atmospheric extinction model is a combination of a basic model of the sources of atmospheric extinction, some prior knowledge of how these sources change with time and location on the sky, and the actual atmospheric extinction profiles of these sources at various airmasses generated using MODTRAN (??).

The shape of the atmospheric transmission curve, $\phi^{atm}(\lambda, alt, az, t)$, is determined by three major sources of atmospheric extinction: molecular scattering (Rayleigh scattering), aerosol scattering (Mie scattering), and molecular absorption.

- Molecular scattering, or Rayleigh scattering, is due to elastic scattering off atoms and molecules in the air. Atmospheric absorption due to Rayleigh scattering has an optical

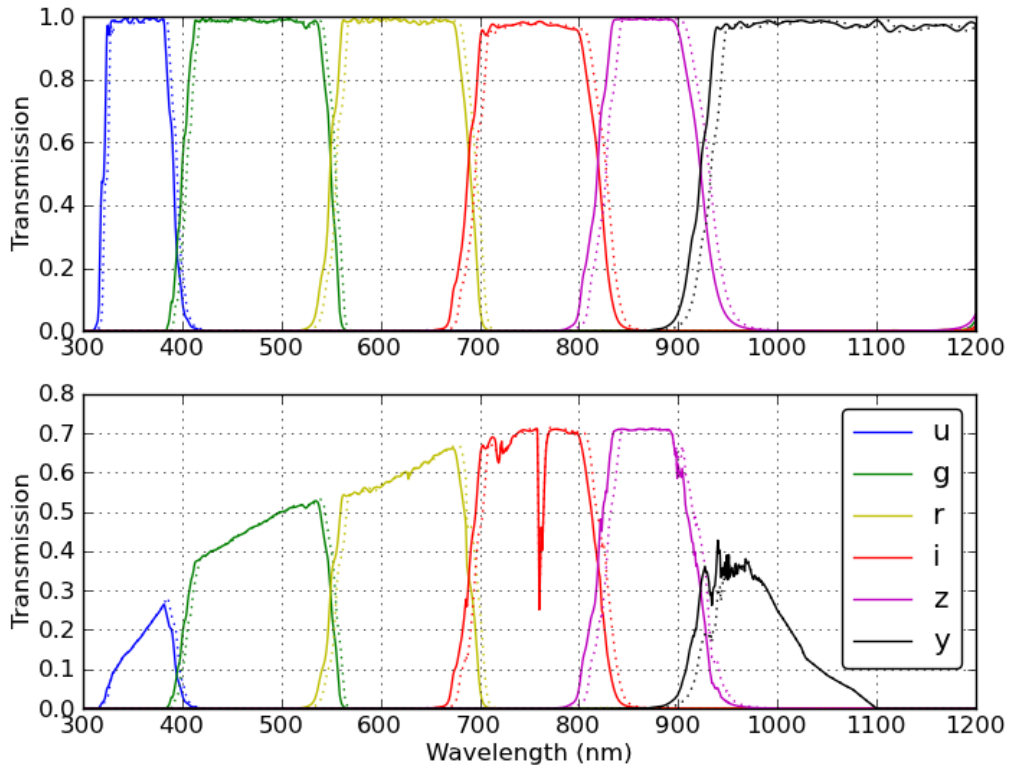


Fig. 9.—: **Baseline filter curves and a potential (1% of the central wavelength) shift due to nonuniformity.** The solid lines indicate standard filter bandpasses (top panel: filter alone, bottom panel: filter plus standard mirror, lens, detector and atmosphere response curves) while the dashed lines indicate the same bandpass shifted redward by 1% of the central wavelength.

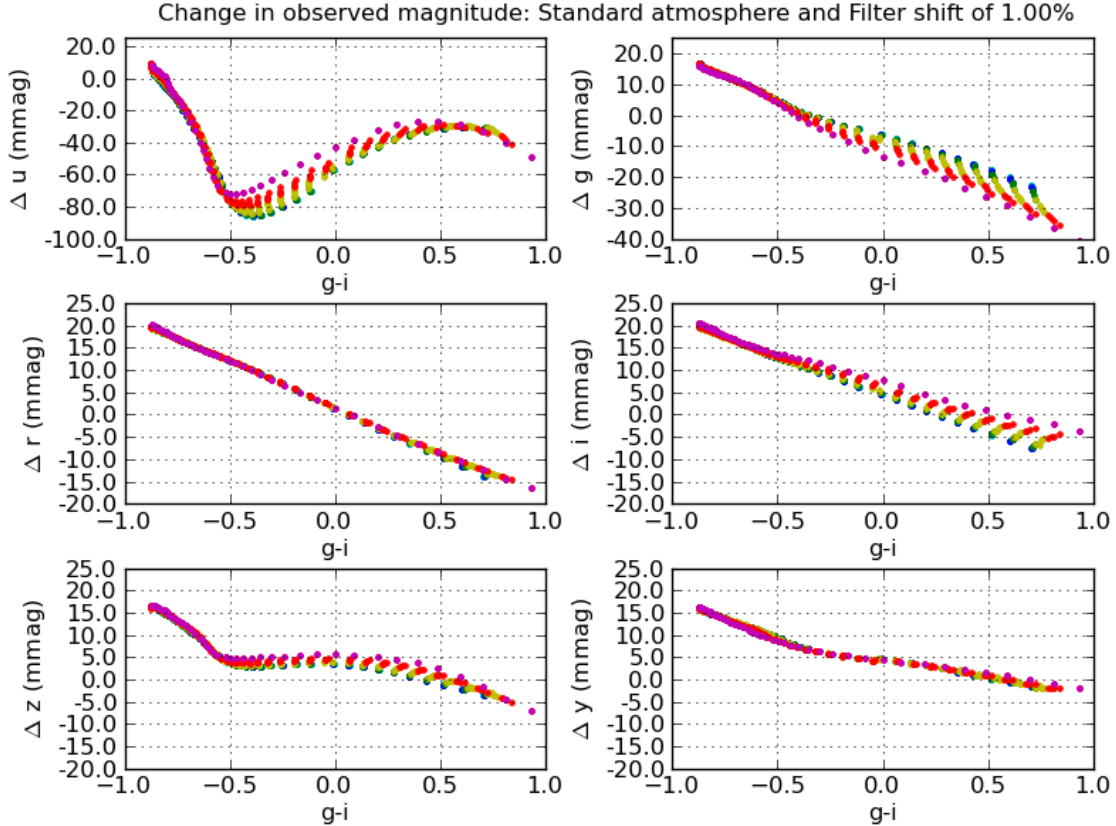


Fig. 10.—: Changes in observed magnitude (measured counts) due to a hardware response curve shift of 1% of the central wavelength of each bandpass. 850 Kurucz models with temperatures between 5000K and 35000K and metallicity indexes between -5.0 and 1.0 (solar) were combined with a standard atmosphere and standard hardware bandpass, and then with a total system response where the atmosphere remained constant but the hardware response was shifted by 1% of the central wavelength of each bandpass (as in Fig 9). Changes in magnitude on the order of 20 mmag are typical, except in u band where the shift can create a δu of closer to 80 mmag for certain kinds of main sequence stars. The points in each plot are color-coded by metallicity, in steps of 1 dex between -5.0 (blue) to 1.0 (magenta).

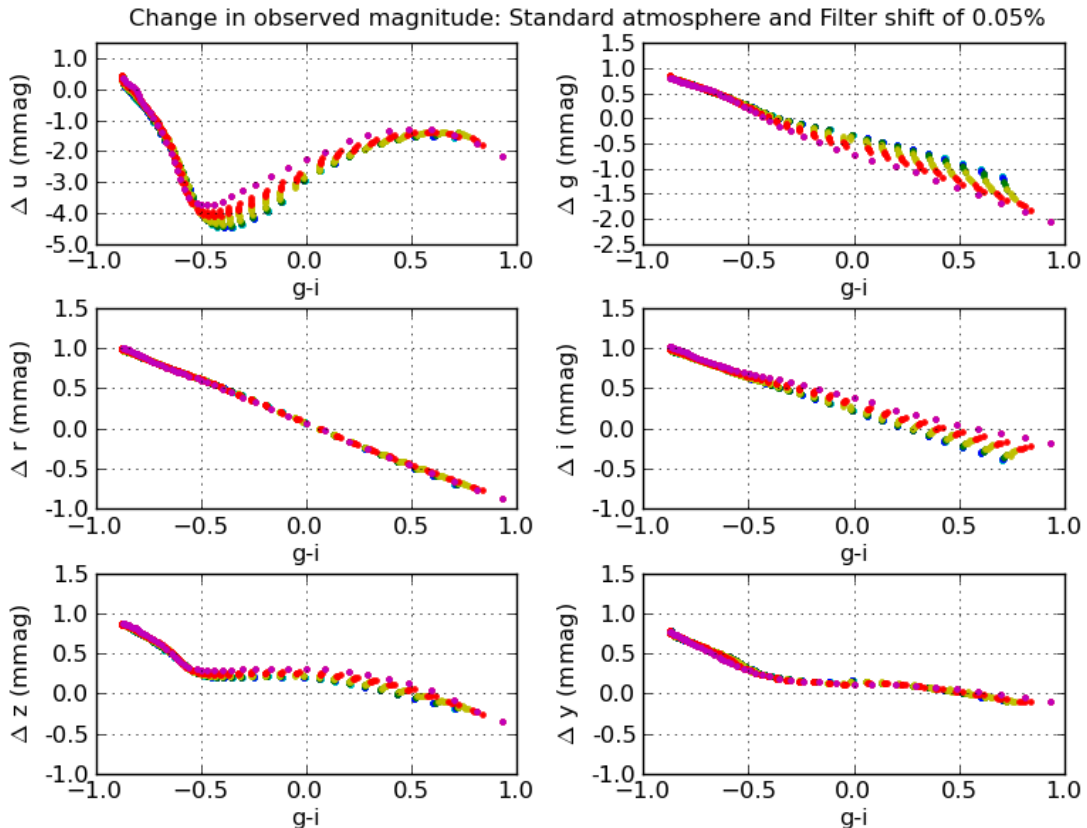


Fig. 11.—: Changes in observed magnitude (measured counts) due to a hardware response curve shift of 0.05% of the central wavelength of each bandpass. Similar to Fig 10 except that the hardware response was shifted by only 0.05% of the central wavelength, an amount representing an unmeasured shift in the hardware response and thus contributing directly to the final error in the calibration of the observed magnitudes. Note that the y scale here is 1/10th of the scale in the previous figure.

depth

$$\tau \propto (\lambda/\lambda_o)^{-4} (BP/BP_o), \quad (17)$$

where BP is the barometric pressure (?), and BP_o is a reference value (typically around 782 mb for Cerro Tololo). The total atmospheric extinction due to Rayleigh scattering is thus driven only by pressure variations and is proportional to airmass,

$$S(\lambda, X) \propto e^{-\tau, X}, \quad (18)$$

and is also axisymmetric around zenith. Changes in the optical depth due to Rayleigh scattering typically will produce < 1 mmag change in the observed counts.

- Aerosol scattering, or Mie scattering, occurs when visible light is scattered by particles suspended in the atmosphere with a size similar to its wavelength. This gives rise to an absorption curve with a strongly variable total column depth as well as a variable wavelength dependence, where

$$\tau \propto (\lambda/675\text{nm})^\alpha. \quad (19)$$

The index α has been measured to range between -0.9 to -1.7 in observations from CTIO (?). From (?) optical depth measurements from Mauna Loa, the total aerosol optical depth at zenith varied from 0 to 0.3 (generally ± 0.1) at $\lambda = 440$ nm, with max rate of change $\approx 0.02/\text{hr}$. The atmospheric extinction due to aerosol scattering scales directly with airmass but is not necessarily axisymmetric around zenith and often has an East-West trend.

- Molecular absorption produces a more complex set of absorption bands and features, originating from line absorption due to ozone (O^3), water (H^2O), oxygen (O^2) and other trace species (OH , N^2O , etc.). The resulting atmospheric absorption features are largely due to narrow saturated Lorentzian-shaped lines spaced closely in wavelength and, due to this saturation, scale non-linearly with airmass,

$$S(\lambda, X) \propto e^{-\tau \sqrt{X}} \quad (20)$$

as in (?). The total column depth for O^2 and other trace species is related directly to the square root of the column depth for molecular scattering, and is thus proportional only to the square root of the barometric pressure and airmass. However, O^3 and H^2O absorption is more variable. O^3 absorption can vary by 5–10% day to day, with seasonal variations of 25% or so, but is expected to be non-variable across the sky and closely correlated with satellite data on total ozone content. H^2O absorption can vary on timescales as short as 10–20 minutes, and is expected to show linear trends across the sky (East-West and North-South).

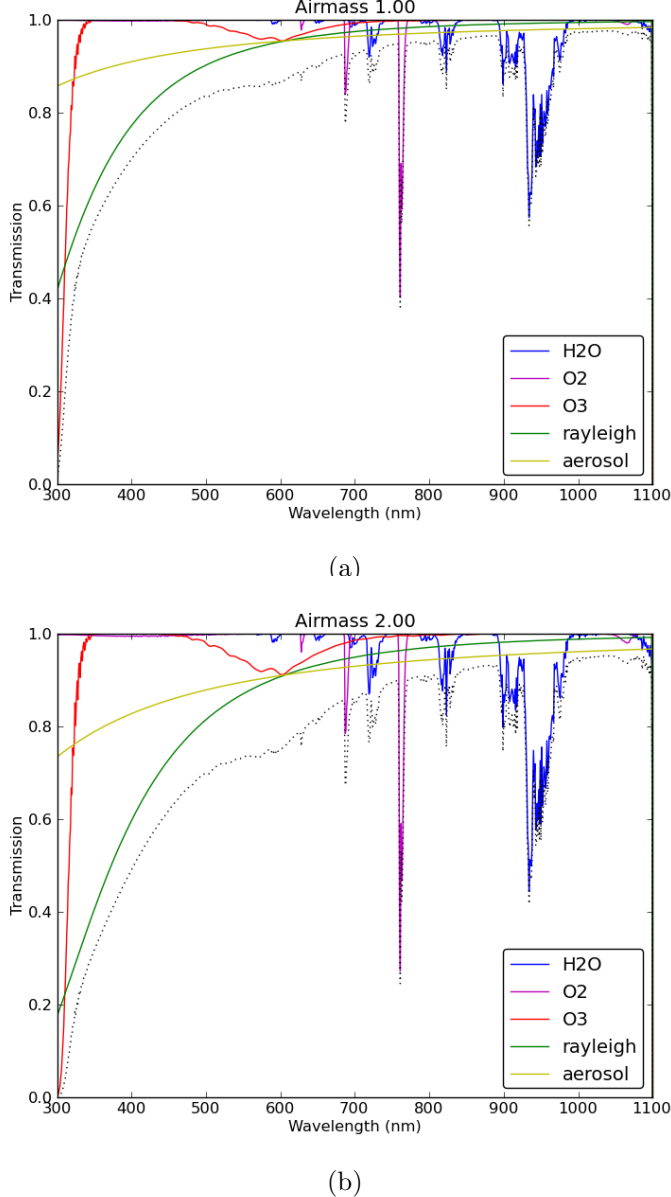


Fig. 12.—: **Components of atmospheric absorption.** The wavelength dependence of the various components of atmospheric absorption at zenith (panel a) and at airmass=2.0 (panel b) is shown here. The H²O(blue) and O³(red) molecular absorption contributions are shown separately, while the O²absorption is combined with other trace elements (magenta). A typical example of aerosol scattering (Mie scattering) is included (yellow), as is molecular scattering (Rayleigh scattering) (green). All components except aerosol scattering were generated using MODTRAN4 with the US Standard option (aerosol scattering is not part of the US Standard atmosphere). The resulting total absorption curve is the product of each of these effects and is shown with the dotted black line. This is an illustrative atmosphere; under actual observing conditions the molecular absorption components will vary in strength with time and the square root of the airmass, the molecular and aerosol scattering will depend on airmass, and the aerosol scattering profile will also vary with time.